Experiments in Fluids 26 (1999) 249–256 © Springer-Verlag 1999

High speed optical tomography system for quantitative measurement and visualization of dynamic features in a round jet

L. McMackin, R. J. Hugo, K. P. Bishop, E. Y. Chen, R. E. Pierson, C. R. Truman

Abstract An optical tomography system that is capable of operating at frame rates of up to 5 kHz has been used to obtain spatially resolved cross-sectional temperature images of a heated round jet. These tomographic images show dynamic details in the evolving vortical flow structures found in the near field of the jet that are consistent with previous studies of low speed jet flow. Reconstructions produced by the system are quantitative temperature distributions of a planar cross section of the jet measuring temperature differences with a spatial resolution of 1.4 mm.

1 Introduction

Optical techniques for the study of flow fields offer advantages over traditional hot-wire anemometry based measurement techniques. Optical measurements are non-intrusive and often yield data in a form that is qualitatively informative as well as quantitative. A variety of optical measurement techniques exist. An excellent review of optical techniques for flow visualization is given by Hesselink (1988). Various optical methods include laser-doppler velocimetry (Durst et al. 1976) for the measurement of velocity at a given spatial point, and particle-image velocimetry, or PIV (Adrian 1991) for velocity measurement over a two-dimensional plane. In PIV only the velocity of marked fluid particles is measured, independent of scalar concentration or density. Laser induced fluorescence (LIF) has yielded detailed planar images of fluid interfaces of high speed flows (Koochesfahani and Dimotakis 1986) and has been used for the investigation of structure and evolution of round jets (Liepmann and Gharib 1992). In Yoda et al. (1994) planar LIF images have been stacked to form x–y volumes from which isoconcentration surfaces can be examined to reveal flow structure. The performance of the LIF measurement depends on the diffusivity of the fluorescent dye that has been added to the flow.

Rather than measuring the velocity or concentration of a seeding material that has been added to the flow as in PIV and LIF, the optical phase of a beam that has propagated through the flow can be measured to yield the temperature or index of refraction, the quantity desired for aero-optical applications. Holographic interferometry (Matulka and Collins 1971; Watt and Vest 1987) has been combined with tomographic reconstruction (Snyder and Hesselink 1988; Watt and Vest 1990) to measure time-averaged and instantaneous three-dimensional scalar fields. However, interferometric and holographic phase measurement tomographic methods require the time consuming analysis of fringe patterns to determine the phase from which to reconstruct images.

In a single-ray phase measurement system related to the multiple-view tomography system described here, beam-deflection tomography has also been used to investigate fluid flows (Faris and Byer 1986). Beam deflection measurements obviate interpreting interferograms to measure optical phase, measuring beam motion instead to obtain the phase gradient. In this technique, gradient measurements are performed electronically using position sensitive detectors. The Hartmann wavefront sensor as described in this paper is an example of an electronic phase gradient sensor.

In general, as the spatial dimension of flow measurement techniques increase, the corresponding increase in the amount of data and necessary processing precludes use of these techniques at high temporal rates. For instance laser doppler velocimetry can operate at tens of kHz, while particle image velocimetry typically works at video rates (30 Hz). Three-dimensional tomography has been limited to discrete snapshots or time-averaged measurements of dynamic flows.

The ability to study the dynamic events that occur in a turbulent flow requires both high spatial resolution in order to capture the features of large scale coherent structures, and high temporal resolution in order to capture the dynamic interaction between these structures. The tomographic system described in this paper is capable of resolving flow field dynamics at rates of up to 5 kHz. Temperature, or equivalently the refractive index or density, is the scalar measured in this technique over a planar cross section of the flow. The intent of this paper is to demonstrate the capabilities of this

Received: *31 July 1997*/*Accepted*: *18 December 1997*

L. McMackin, R. J. Hugo
Air Force Research Laboratory
3550 Aberdeen Ave SE
Kirtland AFB, NM 87117-5776, USA

K. P. Bishop, E. Y. Chen, R. E. Pierson
Applied Technology Associates
1900 Randolph Rd. SE
Albuquerque, NM 87106, USA

C. R. Truman
Department of Mechanical Engineering
University of New Mexico
Albuquerque, NM 87131, USA

Correspondence to: L. McMackin

tomographic system rather than to perform an exhaustive jet flow field investigation. We briefly describe the heated jet flow, concepts in the design and characterization of the tomography system and a comparison of quantitative tomography data to anemometer measurements. We also present typical two-dimensional tomographic flow reconstructions and a three-dimensional volume reconstruction obtained using a conditional sampling technique.

2 Optical tomographic system

The tomographic system is composed of a set of eight one-dimensional Shack–Hartmann wavefront sensors (Neal et al. 1995) arranged at regularly spaced angular intervals in a semi-circular arc around a low speed heated jet. The sensors simultaneously measure the path-integrated phase gradient of laser radiation after it has propagated through a cross section of the near-field of the flow. These path-integrated measurements, called projections, are used as inputs to a standard tomographic algorithm reconstruction (described later in this section) to create two-dimensional images of a cross-section of the flow. The 8-view design, shown schematically in Fig. 1, resulted from a study by McMackin et al. (1995) of reconstructed image quality as a function of the number of projections and Hartmann sensor design parameters.

Each Hartmann sensor is composed of a 2048-pixel linear CCD camera located at the back focal plane of an one-dimensional (1-D) array of 64 small cylindrical lenses that focus light along the axis of the array but do not focus in the orthogonal direction. Each lenslet is 437.5 μm in diameter and has a focal length of 4.0 cm, a design that has been shown to minimize measurement error (McMackin et al. 1995). A collimated laser beam that has propagated through the flow is focused by the lenslets into a linear array of focal lines that are intersected by the CCD pixel array. Phase irregularities in the beam caused by temperature variations in the flow cause shifts to occur in the position of individual focal lines relative to their on-axis positions along the sensor axis. Thus, the focal lines *jitter* as temperature variations in the flow move past the sensor. At any instant in time the displacement of the focal lines along the sensor axis is proportional to the local 1-D tilt on the optical wavefront in the same direction. Each lenslet defines a local subaperture of the sensor over which the average tilt is measured. The CCD camera records the intensity of the focal lines from which the local tilts are calculated. The optical phase differences (OPDs) are obtained by integrating the 1-D tilt measurement over the length of the sensor.

To tomographically reconstruct the index of refraction within the planar area of intersection of these eight views, we employ a variant of the Algebraic Reconstruction Technique (Gordon et al. 1970; Gordon 1974) known as the Simultaneous Iterative Reconstruction Technique, or SIRT (Brooks and Di Chiro 1976; Gilbert 1972). In this iterative method, we reconstruct the image on a square grid of $N \times N$ pixels, starting from an initial guess of constant index of refraction. We rely on the fact that light traveling through the air flow travels along straight paths so that the optical path length measurements are integrals of index of refraction along these paths. For each iteration, i, we calculate projections, $p_k(i)$, by forming a weighted sum of pixels, $n_j(i)$, along the ray path through the reconstruction to the kth wavefront sensing element:

$$p_k(i) = \sum_{j=1}^{N^2} w_{jk} n_j(i) \tag{1}$$

where w_{kj} is a weight proportional to the area of pixel j along ray path k. For each iteration of the algorithm and each projection a new value is calculated for the pixels along the ray path such that the calculated projection matches the measured optical path length, P_k,

$$n_{jk}(i+1) = n_j(i) + \frac{(P_k - p_k(i))\, w_{jk}}{\sum_{j=1}^{N^2} (w_{jk})^2} \tag{2}$$

The values of the pixels are not changed until the end of an iteration, when all projections have been calculated. The new values are the averages over all projections,

$$n_j(i+1) = \frac{1}{M} \sum_{k=1}^{M} n_{jk}(i+1) \tag{3}$$

In simulations of our system performance, 10 iterations were sufficient to converge on a reconstruction with acceptable residual error. Therefore, the results in this paper all represent 10 SIRT iterations. However, it should be noted that our subsequent research suggests that other tomographic algorithms provide significant performance improvements over SIRT for our air flow data.

The sensitivity of the Hartmann sensor is determined by the lenslet f-number (ratio of focal length to lenslet diameter). Since the magnitude of the deflection caused by a given tilt is proportional to the focal length, changing focal length controls sensitivity. In the system described here high sensitivity was required to measure very small tilts on the order of tens of microradians. Lower sensitivity is desirable when large tilts are to be measured. Extensive simulations of the Hartmann sensor

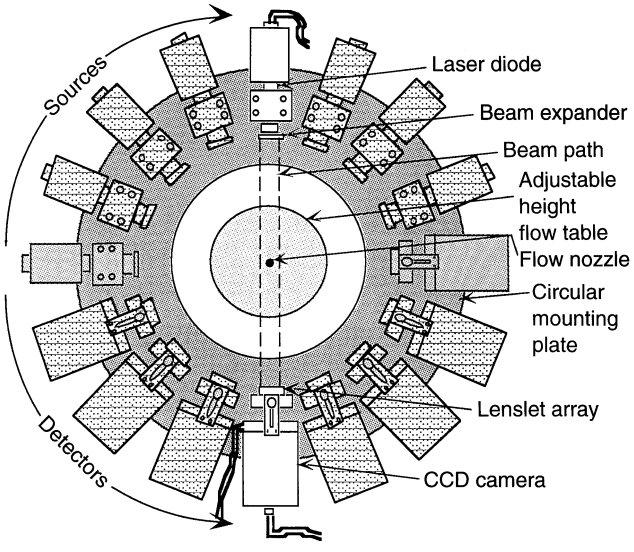

Fig. 1. High-speed optical tomographic system schematic. Eight diode lasers and eight 1-D Hartmann wavefront sensors are arranged around the jet exit

performance (Pierson et al. 1996) used flow field models created from computational jet flow data and flow visualizations. These models were coupled with coherent optical propagation through the lenslet array that accounted for fabrication errors and misalignments, as well as the effects of pixel size, detection noise, digitization, and nearest-neighbor focal spot interactions. From these simulations, the OPD measurement error of a complete sensor was found to be approximately 7 nm, or about one hundredth of a wavelength (at 670 nm). This performance was confirmed by experimental measurements.

Similarly, the operation of the entire 8-view tomography system is simulated by attributing noise to each of the computational projections before image reconstruction. The reconstructed image can be compared to the original model using image quality metrics such as the average, maximum, or RMS error over the entire image. However, as in many image reconstruction applications, the performance of the tomographic imaging system is a function of spatial frequency. Large features within the image are more easily recovered than small features. Because reconstruction noise often manifests itself as high frequency artifacts that can mask lower frequency information in the reconstruction, single-valued metrics can be inconsistent with the actual information content present in the reconstructions. To extract information in the presence of high frequency noise we employed a correlation metric to identify the spatial frequency cutoff for low-pass filtering.

In this metric, shown by Eq. (4),

$$C(\xi)=\frac{[t_\xi \star r_\xi^*]\,(\bar{o})}{\sqrt{[t_\xi \star t_\xi]\,(\bar{o})\,[r_\xi^* \star r_\xi^*]\,(\bar{o})}} \tag{4}$$

the value $C(\xi)$ is defined as the cross correlation coefficient between the band-filtered truth image, t_ξ, and the band filtered reconstruction, r_ξ, where the frequency band occurs within a narrow annular region at radial distance ξ from the origin of the spatial frequency domain. In Eq. (4),* is the complex conjugate, $\star$ indicates the correlation operation, and each of the correlations is evaluated at the origin, $\bar{O}$, assuming the two images have been registered to one another. Both t_ξ and r_ξ are functions of spatial coordinates in two dimensions. This expression can be simplified by recognizing that the correlations in the denomonator of Eq. (4) are the integrals of the power in t_ξ and r_ξ. We use the fact that the value of the functions t_ξ and r_ξ at $\bar{O}$ is the integral of their transforms in the Fourier domain and write the correlation integral as the product of their complex 2-D spatial Fourier transforms (Goodman 1968) to obtain,

$$C(\xi)=\frac{\int_\xi TR^*\,\mathrm{d}\bar{\mu}}{\sqrt{\int_\xi T^2\,\mathrm{d}\bar{\mu}\int_\xi R^2\,\mathrm{d}\bar{\mu}}} \tag{5}$$

In Eq. (5), T and R are the 2-D Fourier transforms of the truth and reconstructed images and the integrals are non-zero only over the narrow angular region ξ in the spatial frequency plane, $\bar{\mu}$. In the discrete approximation appropriate for pixelated images, Eq. (5) becomes

$$C(\xi)=\frac{\sum_{i,j} T_{ij}R_{ij}^*}{\sqrt{\sum_{i,j} T_{i,j}^2 \sum_{i,j} R_{ij}^2}} \tag{6}$$

where the integer pixel coordinates i and j are chosen within one pixel of the frequency ξ.

The narrow band correlation metric can be used to measure the degree of correlation between a model image of the flow and its tomographic reconstruction at many values of the spatial frequency. Correlations are performed within a narrow spatial frequency band for a large range of spatial frequencies present in the images. Typically the degree of correlation decreases with increasing spatial frequency. So, when plotted as a function of spatial frequency, as shown in Fig. 2, these coefficients form a downward sloping curve from which the cutoff spatial frequency of the system can be determined by specifying a minimum acceptable correlation coefficient. A cutoff correlation coefficient of 0.6 (or 60% correlation) was chosen for the 8-view tomography system because the visual quality of typical reconstructions begins to deteriorate when its correlation to the truth image is at or below this value. For typical reconstructions 60% correlation occurs at a spatial frequency around 1.4 mm (see Fig. 2).

Simulating the tomographic reconstruction process using known flow models also allowed us to estimate errors in temperature measurement. The performance of the system after filtering shows that there is a trade-off between resolution in a reconstruction defined by a particular filter cutoff and RMS temperature error. Pierson et al. (1996) have shown that for a reconstruction resulting from the 8-view system, choosing a higher spatial frequency filter leads to slightly higher RMS error, an effect that we believe is due mostly to the restricted number of views. At 2 mm resolution the spatial average error is calculated at 0.6 °C in agreement with lab data. Simulations predict an RMS temperature error of 0.7 °C at that resolution. However, experimental studies have shown that the RMS error can vary by considerably more than this over the reconstructed images. Erroneous temperature fluctuations of up to 4 °C have been found in tomographic reconstructions as compared to anemometer probe measurements at certain points in the flow (McMackin et al. 1997). Our studies have led us to the conclusion that error at points in the reconstruction is sensitive to the surrounding flow structure. We have found that the use of different reconstruction algorithms of produces improved results with the best average and RMS performance being produced when the reconstructions from several algorithms are averaged (Pierson et al. 1998).

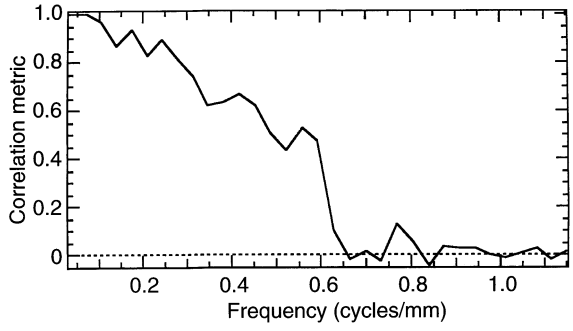

Fig. 2. Correlation metric Eq. (6) plotted as a function of spatial frequency for a typical tomographic flow reconstruction

3
Flow field characterization with optical tomography

3.1
Heated round jet

The flow field facility used to generate the low speed heated round jet is shown in Fig. 3. A variable speed blower forces room temperature air across a heater section and into a plenum chamber. The plenum chamber contains a small recirculating fan to reduce temperature stratification within the plenum. The plenum also includes a recirculating loop that carries air from the plenum back to the blower inlet. This loop is used to maintain a higher flow rate across the heaters than would be produced by exhausting through the 1.27 cm diameter nozzle alone. The air exiting the plenum through the nozzle passes through an aluminum honeycomb and a series of four 20-mesh screens to reduce the turbulence intensity levels at the nozzle exit plane. The overall turbulence intensity at the jet exit, measured as the ratio of the RMS and centerline velocities, varied between 1.2 and 2.9%. The nozzle was machined from solid stock aluminum (23 cm in diameter) with its contour based on a cubic function with zero slope at entrance and exit. The diameter contraction ratio of the nozzle was 15.5:1 over a 24.0 cm length, with an entrance diameter of 19.7 cm and an exit diameter (D) of 1.27 cm.

The centerline temperature of the flow at the nozzle exit is about 10 °C above ambient room temperature, the centerline velocity $U_{cl}=8$ m/s, and the momentum thickness at the nozzle exit plane is 0.17 mm. The Reynolds number based on diameter of this low speed flow is about 5000. Kelvin–Helmholtz instability waves, excited acoustically at the nozzle exit plane, evolve into periodic compact ring vortices. It is these vortices that provide the spatially and temporally evolving index of refraction features that are detected by the optical tomography system. Acoustic excitation by a small speaker located in the plenum directly below the nozzle results in axisymmetric forcing of the shear layer at the nozzle exit plane. Azimuthal modes are excited by a set of eight small speakers flush mounted at the nozzle exit plane (Sapayo and Truman 1997). The forcing frequencies corresponding to the jet column mode and the shear layer mode were determined by non-intrusive linearized stability experiments (Hugo and McMackin 1997). The momentum thickness was determined from the frequency found to produce the most-amplified wave disturbance and the Strouhal number following a procedure described in Browand and Troutt (1985). Using this procedure, the shear layer mode was found to occur at an excitation frequency of 800 Hz and the jet-column mode at 530 Hz. Tomographic measurements of excitation at the jet-column mode and several other frequencies that resulted in unique vortex structures are presented below.

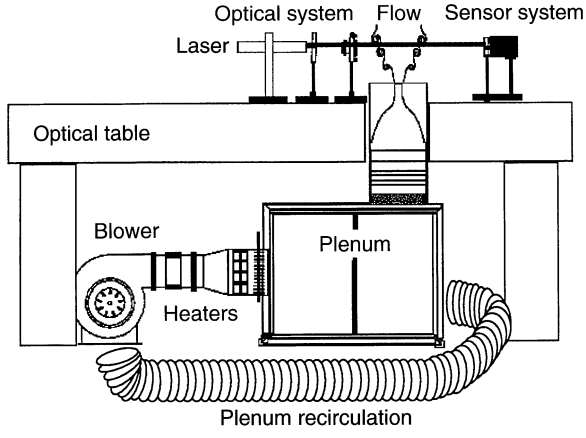

Fig. 3. Jet flow system

3.2
Reconstructions from high speed tomographic acquisition

Several 5 kHz series of tomographic reconstructions of planar cross-sections of the jet are shown in Fig. 4. Although they resemble flow visualizations, these images are actually digital representations of the temperature variations across one plane of the flow orthogonal to the flow direction. In these images, each of the 256 intensity levels corresponds to a specific temperature difference from ambient. A temperature scale is given in the figures.

The sequence of snapshots in Fig. 4a captures images of a distinctive outer ring of hot fluid and an inner ring of entrained cold fluid surrounding the heated core of the flow. These rings are the cross-sections through the rolled Kelvin–Helmholz vortices measured as the flow convects through the data acquisition plane and resemble in form and structure the LIF cross-sectional jet images of Liepmann and Gharib (1992). The sequence shows the periodic passage of these structures across the acquisition plane with a frequency between 263 and 277 Hz, consistent with a forcing frequency of 530 Hz after vortex pairing has occurred.

Using the tomographic imaging technique it is easy to visualize the effect of acoustic forcing on flow structure. Complex flow structure that can only be inferred from anemometry probe measurements can be visually and quantitatively studied using the spatial and temporal resolution of the tomographic system. Figure 4b shows the flow under the influence of a 590 Hz forcing signal where the flow displays a distinctive and persistent pentagonal vortex structure where side jets eject heated air from each corner (Raghu et al. 1990). These jets are related to streamwise vortex structures and therefore persist in the sequence over many snapshots. Figure 4c shows a sequence of images under the influence of azimuthally varying forcing from eight micro-speakers located around the jet exit (Sapayo and Truman 1997). In this case a helical mode structure is established in which the vortex ring appears to "flap" from one side of the jet to the other (Paschereit et al. 1992). This vortex motion is especially apparent when flow reconstructions are shown in a movie at

Fig. 4. Five Kilohertz tomographic reconstruction sequences at (a) 530 Hz, $X/D=2.5$, and (b) 590 Hz, $X/D=2.5$; (c) shows a sequence of images under the influence of azimuthal forcing in which the vortex ring "flaps" from one side of the jet to the other. These image sequences illustrate the spatial and temporal differences between two flow modes excited by different acoustic forcing frequencies. Time increases from left to right within a row and from bottom to top

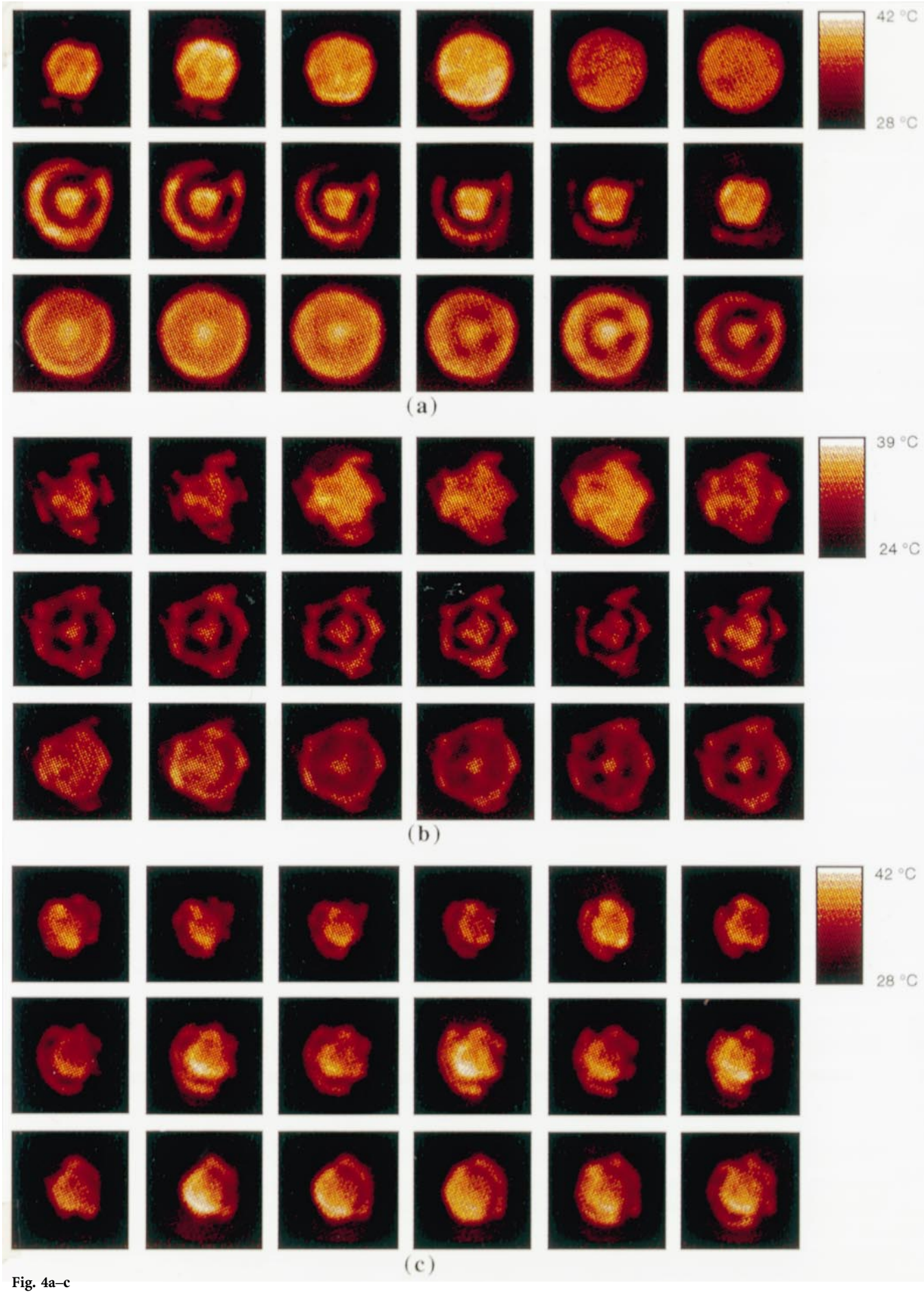

Fig. 4a–c

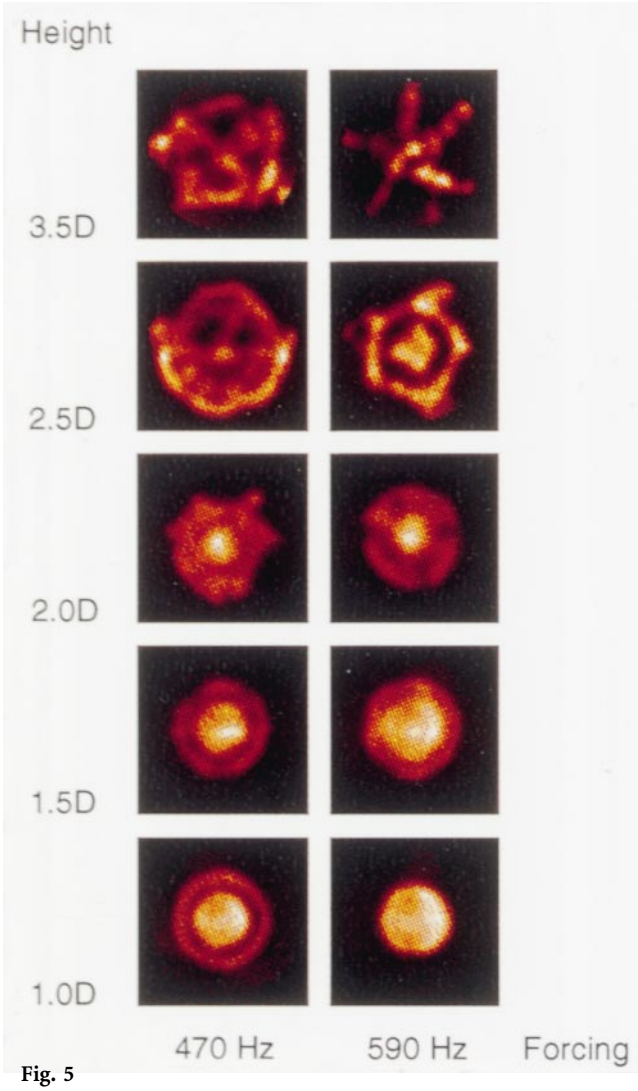

Fig. 5

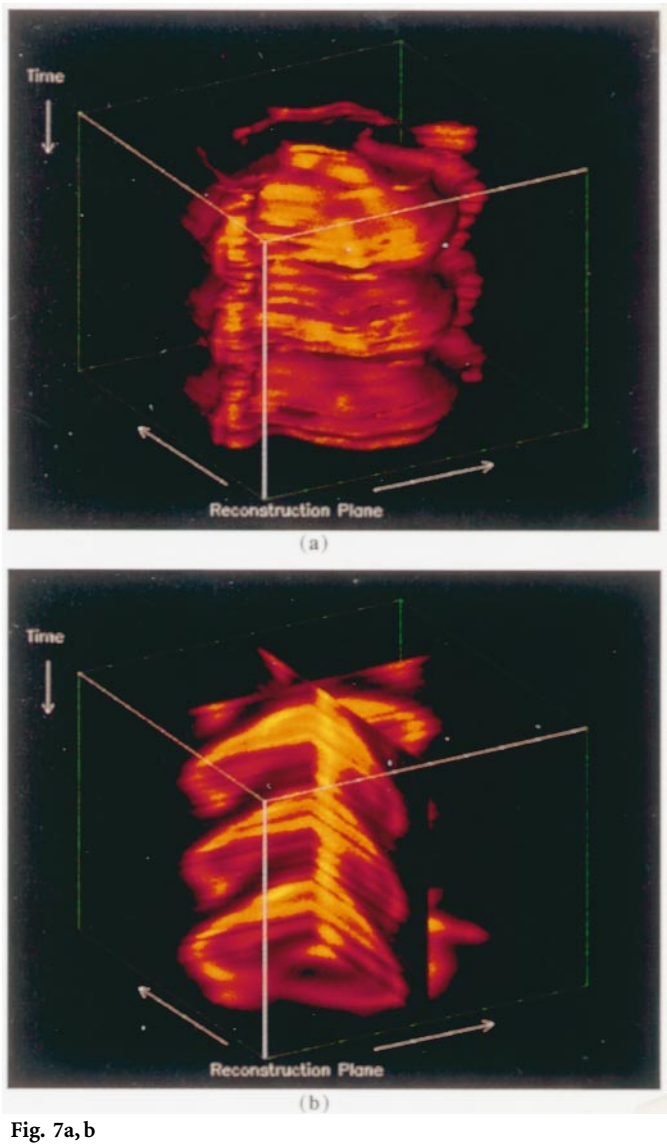

Fig. 7a, b

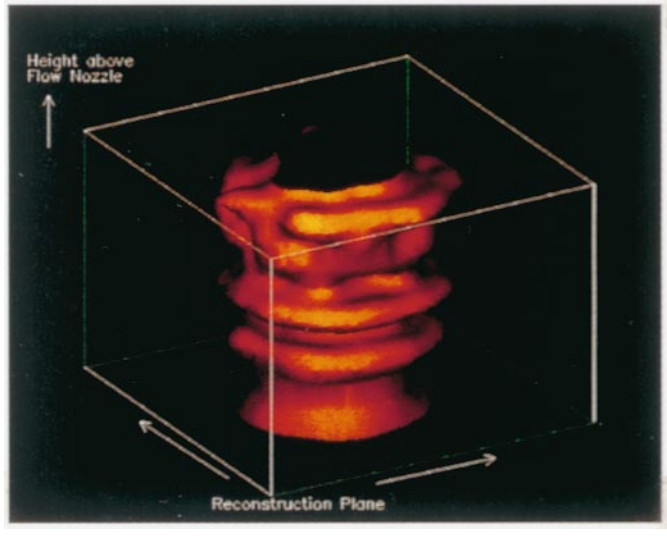

Fig. 8

video frame rates on a computer monitor. Flow sequences shown in this way are useful in visualizing the dynamics of vortex behavior. Actual sequences can be viewed in McMackin et al. (1997).

Previous optical and anemometry studies of the jet flow field have documented that the location and frequency of vortex pairing depends on the applied forcing parameters (Luna et al. 1997). After vortex pairing occurs the shear layer structure increases in size and complexity. Changes in structure are typically inferred by studying the characteristics of the power spectra of optical, velocity, or temperature measurements. In Fig. 5 the structure at different spatial locations in the flow can be directly observed noting the increase in complexity in snapshots from 1.0–3.5*D*, a range over which at least one pairing event is expected to occur. Two forcing frequencies are shown for direct visual comparison of different flow modes.

That the tomography results agree with anemometer measurements quantitatively is shown in the plot of mean temperature in Fig. 6. Temperature measurements obtained from a cold-wire anemometer taken at 64 locations along a diameter through a plane the flow are averaged over a ten second interval. These measurements are compared with the average temperature reconstructed tomographically across the same diameter. To ensure proper convergence, over 10,000 tomographic snapshots are averaged pixel by pixel. Comparison of RMS temperature with anemometry does not agree due to an artifact of the algebraic reconstruction technique that was used to produce the tomographic images as discussed in Section 2. This artifact creates apparent variations in the brightness of the reconstructions from frame to frame creating a difficulty in measuring RMS temperature values. The effects of this artifact can be seen as apparent variations in brightness along the temporal axis in Fig. 7. The suppression of this artifact is currently under study.

Two-dimensional tomographic reconstructions can be stacked to create a time history of the plane of the flow being measured. When plotted as a surface of constant temperature, as in Fig. 7a, such as stack shows at a glance the passage of ring vortex features. As shown in Fig. 7b, a cut through the stack of 64 slices reveals the inner structure of the periodic rolled vortices. Since a cut can be made through the tomographic stack in any direction, we may examine the flow data at any angle.

The stacked LIF images of Yoda et al. (1994) created in their study of the structure and instability modes in natural and forced round jets are composed of slices in the x–y plane that are rapidly scanned along z to produce effectively instantaneous 3-D images. Surfaces of constant concentration of

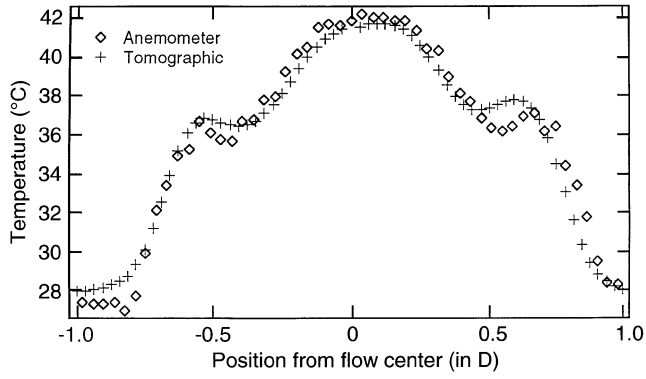

Fig. 6. Comparison of temperature measurements from an anemometer probe traversed across a diameter of the jet flow to a row of pixels across the same diameter of the flow averaged over 10 000 tomographic reconstructions. The point 0.0 represents the center of the flow

fluorescent dye extracted from their stacks show instantaneous distribution of structure rather than the time histories shown in Fig. 7.

Although it is not possible to produce true 3-D from the set of 1-D Hartmann sensors that comprise the tomographic system, it is possible to build 3-D volumes using conditional sampling techniques. To do this, the flow is acoustically excited at the nearly-periodic jet-column mode (530 Hz) and data acquisition is triggered at a specific point in the forcing function. Tomographic snapshots are taken at the same time in the cycle of the forcing function at prescribed downstream locations in the flow (Hugo and McMackin 1996). To produce the volume shown in Fig. 8, conditional data were taken at 11 planes between 1 and 5 cm downstream of the nozzle exit. Sixty-four frames of conditional data were phase averaged at each plane before being stacked. This precise conditional sampling combined with the periodicity of the flow allows the stack to represent a single realization of the flow in three spatial dimensions. Figure 8 shows two vortical structures about to pair in the middle of the volume as well as one larger structure formed from the pairing of two previous structures emerging from the top of the volume. Vortex pairing for this particular forcing condition was found by other tests to occur at an $X/D = 2.25$ in agreement with Fig. 8.

4 Conclusion

In summary, we have devised and demonstrated an optical tomography system capable of measuring two-dimensional temperature (or equivalently, density) profiles of a low speed heated round jet. The data to produce these profiles is acquired at 5 kHz so that tomographic reconstructions achieve high temporal as well as high spatial resolution. Two-dimensional images of the flow are shown in sequential and stacked formats illustrating the visualization quality of our results from the optical tomography system. We have also compared our measurements to traditional anemometry and other flow imaging techniques. Reconstructions produced by the system are quantitative temperature distributions of a planar cross section of the jet whose RMS accuracy at a spatial resolution of

Fig. 5. Tomographic reconstructions illustrating the downstream development of structure in the jet shear layer at two different forcing frequencies

Fig. 7. **a** A stack of 64 tomographic reconstructions shows at a glance the time history of temperature variations that pass through the measurement plane. The spatial plane is represented by the two horizontal axes and time is along the vertical axis. **b** Slicing through the stack reveals the inner details of the flow structure

Fig. 8. Three-dimensional volume created from conditionally sampled tomographic data

2 mm was calculated at 0.7 °C in simulation for the 8-view system. Actual temperature measurement accuracy was found to vary with the complexity of the structure present in the flow and the reconstruction algorithm.

The system was constructed from common electronics and instrumentation. Our system does not push any fundamental limitations in resolution or speed, both of which may be enhanced through custom electronics design. High spatial and temporal resolution in a non-intrusive optical flow measurement system has potential application in wind tunnels, internal combustion studies, and in flows containing complex structure where intrusive probes may be inappropriate. In more restrictive environments where the view of the flow is blocked by walls or other objects, more sophisticated strategies for tomographic reconstruction may be required to compensate for missing data (Cha and Cha 1996). Tomography may also be suitable for the experimental verification of numerical flow models.

References

Adrian RJ (1991) Particle-imaging techniques for experimental fluid mechanics. Ann Rev Fluid Mech 23: 261–304

Brooks RA; Di Chiro G (1976) Principles of computer assisted tomography (CAT) in radiographic and radioisotopic imaging. Phys Med Biol 21: 689–732

Cha DJ; Cha SS (1996) Holographic interferometric tomography for limited data reconstruction. AIAA J 34: 1019–1026

Durst F; Melling A; Whitelaw JH (1976) Principles and Practice of Laser Doppler Anemometry. New York: Academic Press

Faris GW; Byer RL (1987) Beam deflection optical tomography. Opt Lett 12: 72–74

Gilbert P (1972) Iterative methods of the three-dimensional reconstruction of an object from projections. J Theor Biol 36: 105–117

Goodman JW (1968) Introduction to Fourier Optics. New York: McGraw-Hill, p 278

Gordon R; Bender R; Herman GT (1970) Algebraic reconstruction techniques (ART) for three-dimensional electron microscopy and X-ray photography. J Theor Biol 29: 471–481

Gordon R (1974) A tutorial on ART. IEEE Trans Nucl Sci NS-21:78–93

Gilbert P (1972) Iterative methods of the three-dimensional reconstruction of an object from projections. J Theor Biol 36: 105–117

Hesselink L (1988) Digital image processing in flow visualization. Ann Rev Fluid Mech 20: 421–485

Hugo RJ; McMackin L (1996) Conditionally sampled two-dimensional optical wavefront measurements in the near nozzle region of a heated axisymmetric jet. Proc SPIE 2828: 50–61

Hugo RJ; McMackin L (1997) Non-intrusive linearized stability experiments on a heated axisymmetric jet. AIAA Paper 97-1965

Koochesfahani MM; Dimotakis PE (1986) Mixing and chemical reactions in a turbulent liquid mixing layer. J Fluid Mech 170: 83–112

Liepmann D; Gharib M (1992) The role of streamwise vorticity in the near field entrainment of round jets. J Fluid Mech 245: 643–668

Luna T; Truman CR; Masson BS (1997) Linear stochastic estimation of optical beam deflection through a heated jet. AIAA paper 97-0072

Matulka RD; Collins DJ (1971) Determination of three-dimensional density fields from holographic interferograms. J Appl Phys 42: 1109–1119

McMackin L; Masson B; Clark N; Bishop K; Pierson R; Chen E (1995) Hartmann wavefront sensor studies of dynamic organized structure in flow fields. AIAA J 33: 2158–2164

McMackin L; Hugo RJ; Pierson RE; Truman CR (1997) High speed optical tomography system for imaging dynamic transparent media. Opt Express 1: 302–311 http://epubs.osa.org/oearchive/source/2360.htm

Neal D; Pierson RE; Chen EY; Bishop KP; McMackin L (1995) One-dimensional wavefront sensor development for tomographic flow measurements. SPIE Proc. 2454: 375–390

Paschereit CO; Oster D; Long TA; Fiedler HE; Wygnanski IJ (1992) Flow visualization of interactions among large coherent structures in an axisymmetric jet. Exp Fluids 12: 189–199

Pierson RE; Chen EY; Bishop KP; McMackin L (1996) Modeling and measurement of optical turbulence by tomographic imaging of a heated air flow. SPIE Proc. 2827: 130–141

Pierson RE; Olsen DF; Chen EY; McMackin L (1998) Comparison of reconstruction algorithm performance for optical phase tomography of a heated air flow. Submitted to Appl. Opt.

Raghu S; Lehmann B; Monkewitz PA (1990) On the mechanism of 'side-jets' generation in periodically excited axisymmetric jets. In: Advances in Turbulence, Vol. 3, pp 221–226. Berlin: Springer

Sapayo J; Truman CR (1997) Study of the development of axisymmetric and helical modes in heated air jets using fast optical tomography. AIAA Paper 97-1809

Watt DW; Vest CM (1987) Digital interferometry for flow visualization. Exp Fluids 5: 401–406

Watt DW; Vest CM (1990) Turbulent flow visualization by interferometric integral imaging and computed tomography. Exp Fluids 8: 301–311

Yoda M; Hesselink L; Mungal MG (1994) Instantaneous three-dimensional concentration measurements in the self similar region of a round high Schmidt number jet. J Fluid Mech 279: 313–350